Progress In Electromagnetics Research, Vol. 175, 91–104, 2022

Low-Profile High-Gain Wideband Multi-Resonance Microstrip-Fed Slot Antenna with Anisotropic Metasurface

Enyu Zhou[1], Yongzhi Cheng[1, *], Fu Chen[1], Hui Luo[1], and Xiangcheng Li[2, *]

Abstract—In this work, a high-gain and wideband microstrip-fed slot antenna is proposed and investigated, which is composed of an anisotropic metasurface (AMS) and an aperture coupled structure. The proposed microstrip antenna with four resonances can be obtained by merging the AMS with an anomalous inverted π-slot feed structure in a low profile ($1.07\lambda \times 1.07\lambda \times 0.06\lambda$). The simulated results indicate that the proposed microstrip antenna can achieve a wide impedance bandwidth of 56.1% from 3.32 to 5.91 GHz, which is verified by experiment. In addition, the measured results show that the peak gain of the proposed microstrip-fed slot antenna is 10.7 dBi at 5.3 GHz, and the relative bandwidth of 3-dBi gain is 42.2% from 3.85 to 5.91 GHz. Compared with previous works, the proposed design has a lower profile while achieving a much wider operating bandwidth, where the four controllable resonance modes offer more possibilities for band expansion. This work shows potential application in integration with high data rate systems.

1. INTRODUCTION

Nowadays, there is an increasing demand for high speed, accurate, and seamless signal transmission with the rapid development of 5G communication systems, which requires wideband, high-gain, and low-profile antennas for easy integration [1]. Microstrip technology has fascinated many antenna researchers over the last few decades since it can achieve low profile, low cost, easy preparation and integration [2]. However, traditional designs are usually limited by narrow bandwidth and low gain, which are difficult to accommodate the requirements of modern 5G communication systems. Designing compact antennas with a wide bandwidth and good radiation performance is therefore a challenge. Many effective methods of bandwidth optimization have been proposed intensively, such as increasing substrate thickness [3], aperture coupling feeding [4], multi-layer metallic-dielectric array radiator [5], double dipole with stubs [6], or fractal geometry [7]. Meanwhile, several schemes for antenna gain optimization have also been proposed, such as the use of parasitic patches [8], shorted pins [9], array technology [10], and Fabry-Perot resonator cavity [11]. For example, Cao et al. simultaneously achieved a broadband impedance bandwidth of 41.8% (at 15.05 GHz) and a peak gain of 10 dBi by combining two radiating edges of the main radiation patch with a pair of parasitic mushroom arrays [12]. Nevertheless, most of the works mentioned above exhibit undesired high operating bands, profile, or polarization levels.

Metasurfaces (MSs), as quasi two-dimensional (2D) planar forms of metamaterials (MMs), have been extensively used in antenna design due to their unique electromagnetic (EM) response properties of efficient selective absorption [13], gain amplification [14–18], bandwidth optimization [19–21], filtering response [22, 23], polarization conversion [24–29], etc. It is found that using a microstrip aperture coupled feed structure as an excitation element for the MSs can achieve the efficient optimization of

---

Received 22 June 2022, Accepted 25 August 2022, Scheduled 16 September 2022

* Corresponding author: Yongzhi Cheng (cyz0715@126.com), Xiangcheng Li (lixiangcheng@wust.edu.cn).

[1] School of Information Science and Engineering, Wuhan University of Science and Technology, Wuhan 430081, Hubei, P. R. China.

[2] The State Key Laboratory of Refractories and Metallurgy, Wuhan University of Science and Technology, Wuhan 430081, P. R. China.

other parameters while preserving the low-profile characteristics of the antenna structure. For example, Liu et al. proposed an MMs-based microstrip-fed slot antenna composed of an array of mushroom cells with ground plane, which could obtain an operating bandwidth of 25% and a peak gain of 9.9 dBi [30]. Subsequently, they constructed a periodic array of tandem capacitors loaded with MMs by slotting in radiating patches and coupling slot in the floor, achieving an operating bandwidth of 28% and a peak gain of 9.8 dBi [31]. Majumder et al. proposed a wideband microstrip antenna using a pair of feed slot structures and an MS layer composed of periodically arranged rectangular rings, which could achieve an impedance bandwidth of 14% with a peak gain of 10.5 dBi [32]. Bai and Wang proposed a tri-band microstrip antenna by combining two superimposed layers of the same size with a diamond-shaped array and an aperture coupling feed structure, which could achieve relative bandwidths of 7.8% at 4.36 GHz, 3.6% at 5.02 GHz, and 41.1% at 6.81 GHz, respectively [33]. However, the approaches proposed above still leave a significant scope for expansion in the sub-6 GHz band.

In this paper, a high-gain wideband microstrip antenna composed of an AMS and an inverted π-slot coupled feed structure is proposed and demonstrated in microwave region. By efficiently arranging the unit-cells of the anisotropic metasurface (AMS) and combining an inverted π-slot coupled feed structure, multiple successive resonance points can be obtained, and a broadband high-gain radiation of the MS antenna can be achieved. The architecture of the work is organized as follows. In Section 1, the research background and significance of the antenna are briefly described. In Section 2, the resonance principle and phase response of the proposed AMS are explored, and then the resonance modes of the proposed structure are numerically illustrated. In Section 3, numerical simulations as well as experimental measurements are carried out to verify the radiation performance of the proposed antenna. Finally, the conclusion and outlook are given in Section 4.

2. ANTENNA CONFIGURATION AND OPERATION MECHANISM

2.1. AMS Structure Design and Analysis

In order to elucidate the resonance response mechanism of proposed AMS to the incident different linear polarization waves, a unit-cell structure was constructed as shown in Fig. 1. The unit-cell of the designed AMS consists of a metal resonator structure and metal ground plane separated by a dielectric substrate. The FR-4 (lossy) with relative permittivity of 4.3 and loss tangent of 0.025 is selected as the dielectric substrate in this design. The surface metal resonator structure of the unit cell is constructed by etching a pair of multistage slots on the surface of a conventional square copper patch, as shown in Fig. 1(a). Geometric parameters of the unit-cell structure are given as: $p = 11.4$, $w = 5$, $a = 10$, $b = 0.5$, $c = 1$, $d = 1.4$, $e = 1.4$, and $h_1 = 3$ (all dimensions in mm).

According to the analysis of Sievenpiper et al., the resonance frequency of the unit cell usually coincides with zero-reflection-phase point [34, 35]. At low frequencies, the reflection phase is π, where the unit cell behaves like a normal conventional rectangular metal surface. As the frequency increases, the reflected phase slopes downwards, eventually passing zero at the resonance frequency. Above the resonance frequency, the phase returns to $-\pi$. In order to explore the polarization-dependent property of the proposed AMS structure, the phase response for the normal incident x- and y-polarization waves was investigated as shown in Fig. 1(c). The numerical simulation of the proposed AMS structure was carried out by the method of moments in the spectral domain in CST Microwave Studio (MWS). The unit-cell boundary conditions were used in the x- and y-axis directions of the unit cell to simulate an infinite periodic structure of MS with a Floquet port at the front side along the z-axis direction.

For comparison, the reflection phase angles of the conventional square patch for the normal incident x- and y-polarization waves were also simulated. Owing to its geometric symmetry of the square patch, the corresponding reflection phase angles are the same for the normal incident x- and y-polarization waves, e.g., $\mathrm{Arg}(r_{xx}) = \mathrm{Arg}(r_{yy})$, as shown in Fig. 1(c). Nevertheless, the surface currents excited at the surface of the unit cell of the proposed AMS structure have different lengths of paths for the normal incident x- and y-polarization waves. As shown in Fig. 1(c), for the normal incident y-polarization wave, the conventional square patch and proposed unit-cell excite similar current paths lengths, resulting in similar resonance responses around 5.5 GHz. However, in the case of the normal incident x-polarization wave, a significant redshift of resonance frequency occurs due to the longer surface current path excited by the proposed AMS structure. It produces resonance responses at 4.58 GHz and 5.35 GHz for the

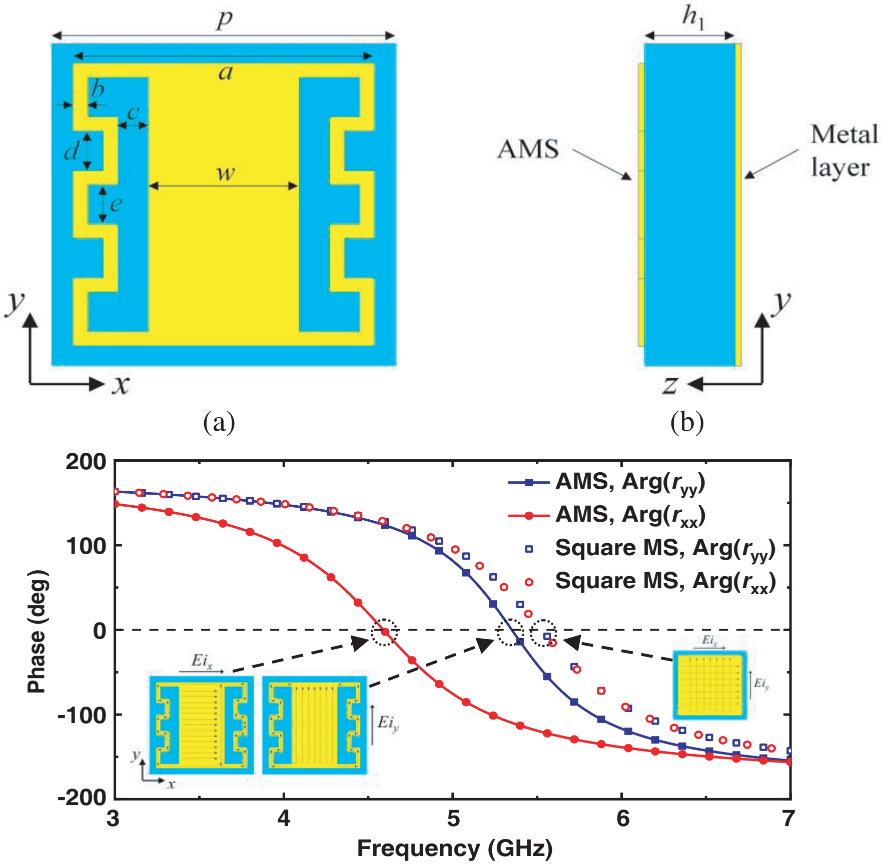

(a) (b) (c)

Figure 1. The (a) front and (b) lattice view of the unit cell, (c) the simulated reflection phases of the square patch and the proposed unit cell for the normal incident x- and y-polarization waves.

normal incident x- and y-polarization waves, respectively. By arranging the unit-cell structures orderly along x- and y-axis directions, two adjacent resonance responses can be obtained simultaneously. It means that this design method can be used to achieve dual-mode resonance wideband characteristics of AMS.

2.2. Multi-Resonance Antenna Design and Operation Mechanism

According to the analyses of polarization-dependent reflection-phase features of the proposed AMS structure, it can be found that different resonance modes can be inspired by arranging the AMS unit cells along different orientations. To demonstrate this design concept, the proposed AMS array is combined with a coupling slot to realize a wideband high-gain multi-resonance AMS antenna.

The configuration of the proposed antenna was given in Fig. 2. As shown in Fig. 2(a), the proposed AMS consists of an array of 4 × 4 unit-cells ordered in the x- and y-axis directions, and is printed on an FR-4 (lossy) dielectric substrate. From Fig. 2(b), the aperture coupled structure is mainly made of an inverted π-slot etched at the center of the metal ground-plane, which is combined with a microstrip feed line. As shown in Fig. 2(c), the proposed design is a three-layer structure where the feeding part is constructed on the same dielectric substrate as the AMS. After optimization, geometric dimensions are given as: $L = 70$, $g = 1.4$, $l_s = 34$, $d_l = 14$, $d_{s1} = 26$, $d_{s2} = 20.4$, $w_{s1} = 2.8$, $l_{d1} = 2$, $l_{d2} = 41$, $w_{d1} = 8$, $w_f = 1.8$ and $h_0 = 1$ (the dimension is all in mm).

As the microstrip line excites the electric fields along the y-axis direction, surface currents will be generated in the same direction on the surface of the proposed AMS structure. Depending on the

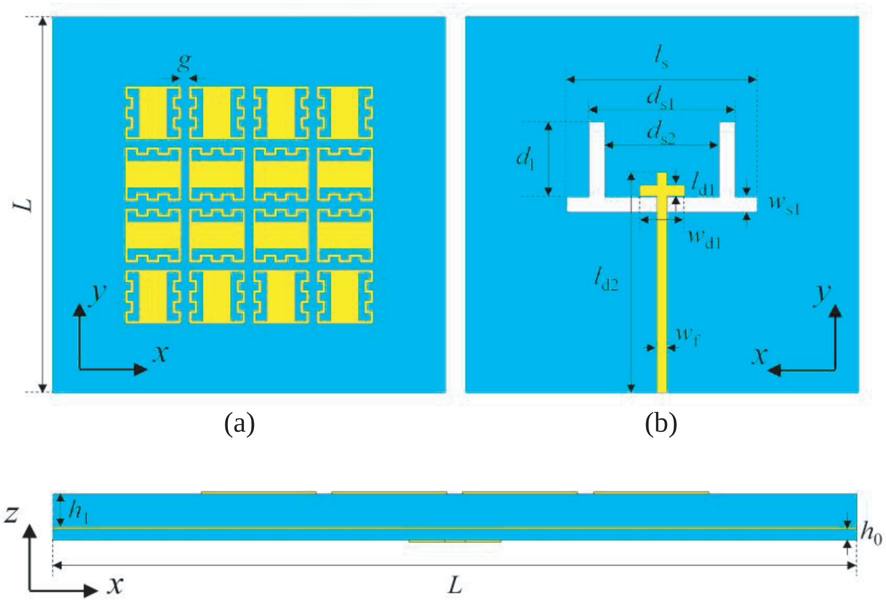

(a) (b)

(c)

Figure 2. (a) Front view, (b) back view and (c) lattice view of the proposed AMS-based microstrip-fed slot antenna.

polarization-dependent property of the unit-cell structure, the surface currents of vertically aligned unit cells will be excited by electric fields in the same direction with two current paths of different lengths, resulting in two resonance responses. As the directivity of the radiation from the single aperture coupled structure is more concentrated along the z-axis direction at the lower frequency and diverges in the positive and negative y-axis directions at the higher frequency region, the unit cells with longer excitation current paths are placed in the two central rows, while those with shorter excitation current paths are placed on the sides. Thus, unit cells are fully excited at different resonance frequencies. In conjunction with the previous discussion, the arrangement of unit cells can significantly affect the radiation performance of the antenna. To further elucidate the proposed AMS-based microstrip-fed slot antenna, the one with four different MS types and arrangements of unit cells with same dimension as shown in Fig. 3 was constructed for comparison. All of those structures are constructed on FR-4 (lossy) dielectric substrates with copper patches [36].

The constructed Antennas 1, 2, and 3 are presented as references to further explore the resonance characteristics of the proposed AMS structure. As shown in Fig. 3(a), Antenna 1 consists of a conventional 4×4 square patch array as its radiation part, where the dimension of the patch is the same as the proposed unit cell. From Figs. 3(b), (c), the proposed 4×4 unit-cells of the MSs of Antennas 2 and 3 are arranged along the x- and y-axis directions, respectively. For comparison with the proposed antenna, the three reference antennas all use an identical microstrip aperture coupled feed structure, and the spacing of unit cells is the same. The performances of the reference antennas and the proposed one are represented in Fig. 4. As can be seen in Fig. 4(a), the proposed antenna has four resonance frequency points (f_1-f_4), located at 3.5 GHz, 4.77 GHz, 4.93 GHz, and 5.67 GHz, respectively, with a better wideband impedance bandwidth of 56.1% from 3.32 to 5.91 GHz than the three reference antennas.

Figure 4(b) represents the gain performance of the antennas with four different MS structures, where the proposed AMS-based antenna achieves the highest peak gain as well as effective and stable radiation at the higher frequency region. In addition, the proposed antenna structure provides an effective gain along the propagation direction at all four resonance points, which results in a good continuous radiation over the entire operating band.

Notably, since the lower frequency resonance f_1 (3.5 GHz) is mainly provided by the excited coupling inverted π-slot on the ground plane, all structures resonate around f_1 after loading the MS with the same dimensions. However, the unit cells of Antennas 1 and 2, aligned in single direction, respectively, lack

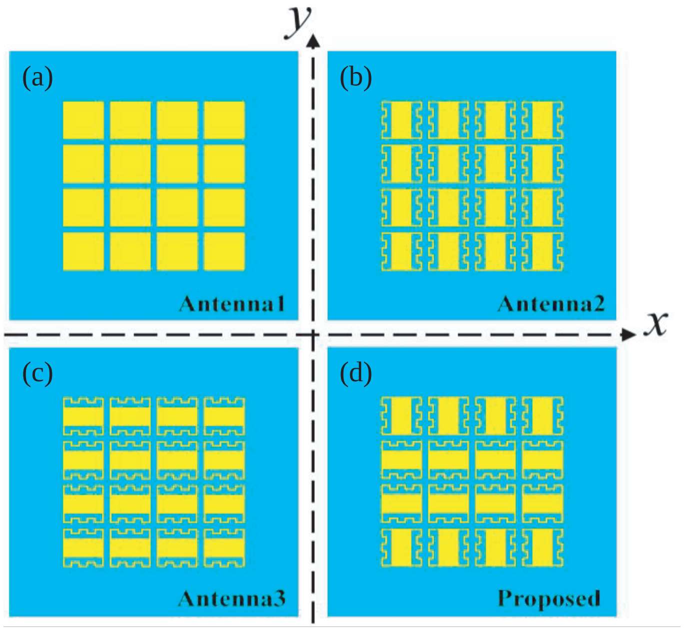

Figure 3. Schematic diagrams of microstrip-fed slot antennas with different MS array.

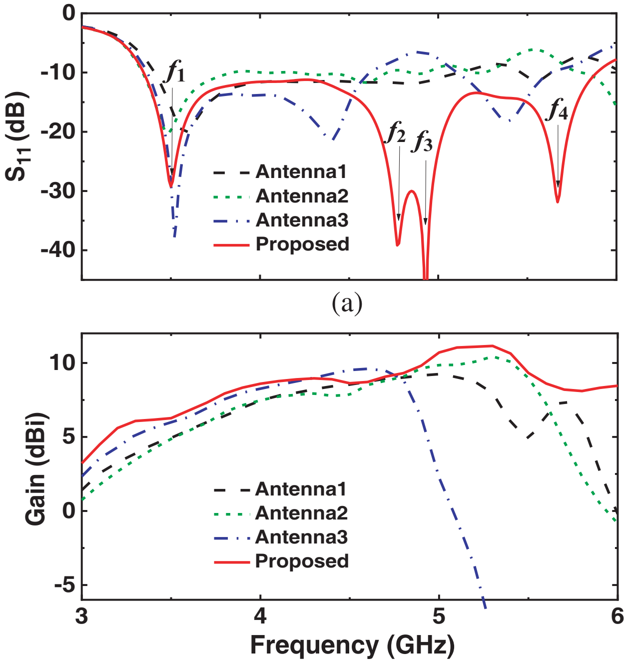

(a)

(b)

Figure 4. Comparison of (a) reflection coefficient (S_{11}) and (b) gain of antennas with different MS types and arrangement of unit cell structure.

the lower frequency resonance response to the incident y-polarization waves and exhibit poor reflection coefficient. Although the arrangement of MS of Antenna 3 produces a resonance response to the incident y-polarization waves near the lower frequency, its gain performance is undesirable due to the lack of resonance response at the higher frequency.

The input impedance of the proposed antenna structure is given in Fig. 5, where it can be seen

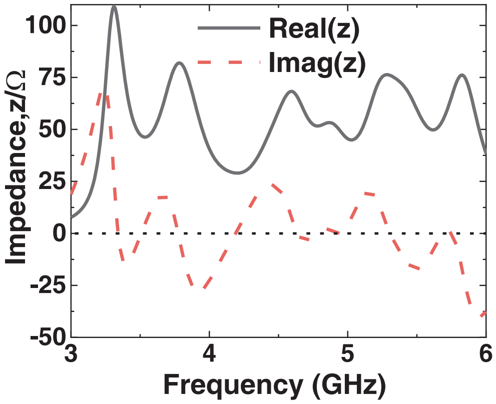

Figure 5. Simulated results of the real and imaginary parts of the input impedance of the proposed antenna structure.

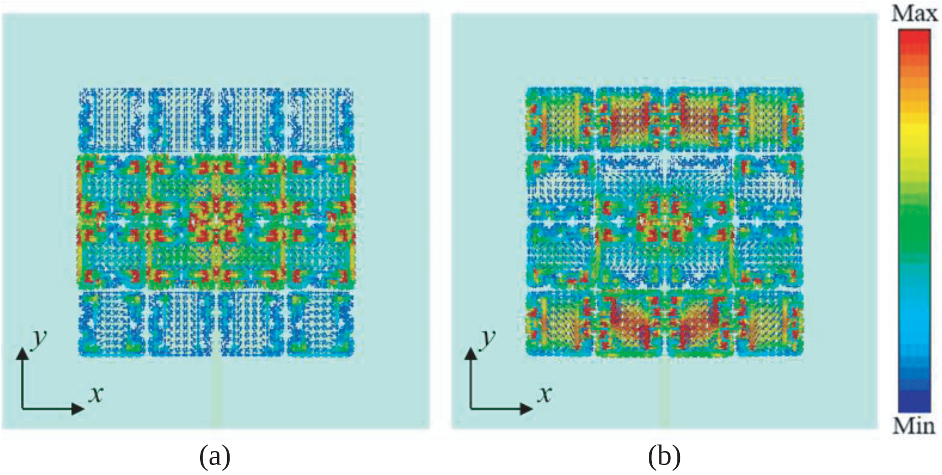

(a) (b)

Figure 6. Simulated surface current distributions of the proposed AMS array at (a) 4.77 GHz and (b) 5.67 GHz.

that the real part of the proposed antenna is about 50 Ω at different resonance frequencies, while the imaginary part is near 0. It means that the input impedance of the proposed antenna structure is matched well with the microstrip-fed line. Thus, we can expect that the proposed antenna structure should have a better radiation performance in our interested frequency range.

To explore the operating mechanism of the proposed design, the surface current distributions at four resonance frequencies are depicted in Fig. 6 and Fig. 7, respectively. The surface currents on the AMS array at the two resonance frequencies ($f_2 = 4.77\,\text{GHz}$ and $f_4 = 5.67\,\text{GHz}$) have essentially uniform vectors, but the amplitudes behave differently. At the second resonance f_2 (4.77 GHz), the surface currents on the middle two rows of horizontal unit cells are predominantly excited, while the current amplitude in the upper and down area is smaller. On the contrary, the surface currents of the unit cells of the upper and down marginal area are mainly excited at the fourth resonance f_4 (5.67 GHz). At the same time, the surface energy is fully concentrated and radiated by different rows of the AMS unit cells at the corresponding frequencies, which allows the antenna structure to exhibit a high gain at the above two resonance frequencies. It can be seen clearly that for the incident y-polarization waves, the center unit cells with the longer excited current path is mainly responsible for the radiation at the second resonance f_2, while the marginal unit cells with the shorter excited current path is mainly responsible for the radiation at the fourth resonance f_4. The simulation results were consistent with the analysis of the unit cell and demonstrated the feasibility of the proposed AMS structure to excite

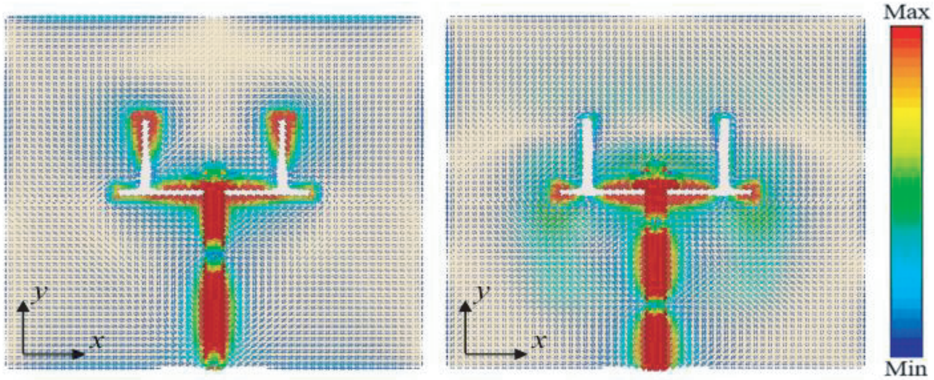

(a) (b)

Figure 7. Simulated surface current distributions of the microstrip aperture coupled feed structure at (a) 3.5 GHz and (b) 4.93 GHz.

dual-mode radiation. It means that the second and forth resonance modes are mainly determined by the designed AMS. By loading a pair of symmetrical multistage stubs on a conventional rectangle slot of the AMS structure, two radiation modes (f_2 and f_4) can be achieved. To further investigate the radiation mechanism of the proposed design, the surface current distributions of the microstrip aperture coupled feed structure at the first f_1 (3.5 GHz) and third resonances f_3 (4.93 GHz) are given in Fig. 7.

The microstrip aperture coupled feed structure of the proposed antenna is made of an inverted π-slot and a microstrip feed line separated by an FR-4 (lossy) substrate. The inverted π-slot was fed by a microstrip line located on the back of the substrate. The height of the inverted π-slot is d_l. When $d_l = 0$, only the full-wavelength mode, i.e., the main radiation mode is excited, as shown in Fig. 7(b). At this point, the surface currents are mainly concentrated at the edge of the rectangle slot, which excites the main radiation mode. The length of inverted π-slot will affect the third resonance mode, and the corresponding resonance frequency f_3 can be expressed approximately as [10, 31]:

$$f_3 \approx c/(l_s\sqrt{\varepsilon_{re}}) \tag{1}$$

$$\varepsilon_{re} = (\varepsilon_r + 1)\Big/2 + \left(1\Big/\sqrt{1 + 12h_0/w_f}\right)(\varepsilon_r - 1)/2 \tag{2}$$

where c is the free-space speed of light, ε_{re} the equivalent permittivity, and ε_r the relative permittivity of the dielectric substrate. By bringing in the relevant parameters, it is calculated that ε_{re} equals 3.25, and f_3 is approximately located at 4.90 GHz, which agrees with the simulation. When d_l increases gradually, the extra radiation mode is introduced, and the current distribution of the inverted π-slot is displayed in Fig. 7(a). In this case, the surface currents are mainly concentrated at the edge of the inverted π-slot, which is mainly provided by a part of the main radiation mode. The inverted π-slot will affect the first resonance mode, and the corresponding resonance frequency f_1 can be approximately expressed as [10]:

$$f_1 \approx c\Big/\left[(d_{s1} + 2d_l)\sqrt{\varepsilon_{re}}\right] \tag{3}$$

By calculation, f_1 is approximately located at 3.26 GHz, which is close to the simulation one. Since the center part of the rectangle slot gathers more currents than the slot stubs, the radiation patterns from the inverted π-slot can remain stable. It can be clearly seen that the feed structure has two different radiation modes. And the two modes are independent of each other at various resonance frequencies, resulting in the improvement of wideband performance.

The resonance modes are mainly determined by the slot length l_s and height d_l of the inverted π-slot, and the effects on the reflection coefficient (S_{11}) for the variation of the parameters are depicted in Fig. 8. As shown in Fig. 8(a), when the length l_s of the inverted π-slot structure is increased gradually, the frequency of the third resonance f_3 decreases steadily, while the overall S_{11} of the antenna deteriorates progressively. In order to obtain a wider operating frequency and a stable S_{11}, l_s was set as 34 mm in this design. It is worth noting that with the change in the third frequency f_3, the resonance response of

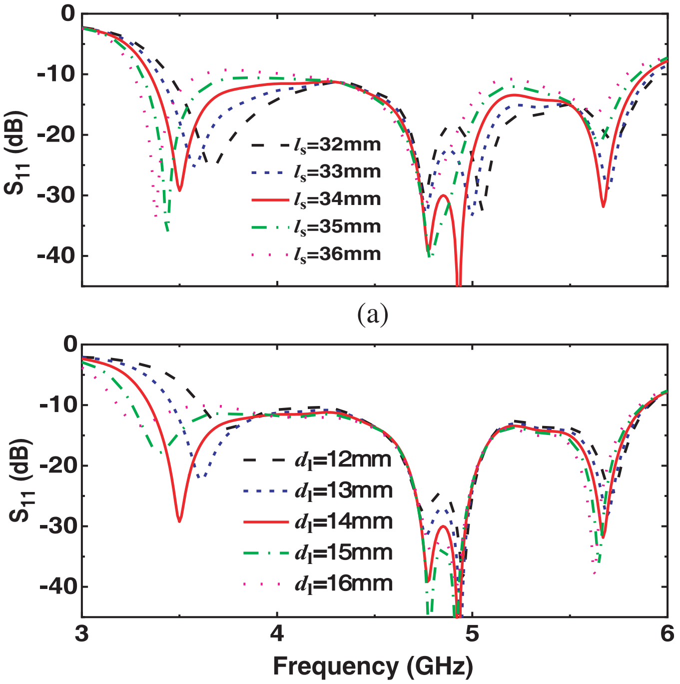

(a)

(b)

Figure 8. Effect of (a) l_s and (b) d_l of the inverted π-slot structure on the reflection coefficient (S_{11}) of the proposed microstrip antenna.

the inverted π-slot will be affected by the main radiation mode resonance, resulting in a red-shift in the first resonance f_1 as well as when l_s is increased. In contrast, when the height d_l of the inverted π-slot is increased gradually, only the first resonance frequency f_1 as the extra radiation mode resonance is significantly shifted. To balance the S_{11} and operational bandwidth, d_l was set as 14 mm in this design.

3. MEASUREMENT RESULTS AND DISCUSSION

For proving the design conception, the prototype of the proposed AMS-based microstrip-fed slot antenna was fabricated by the traditional printed-circuit-board (PCB) technology, and further measurements and discussions were implemented. Fig. 9 presents photographs of the fabricated design, including three layers of the AMS array, coupled inverted π-slot, and microstrip feed line, which are made of copper and separated by FR-4 (lossy) substrate.

Simulated and measured S_{11} and realized gain results of the proposed antenna are presented in Fig. 10 for comparison and verification. The results of return loss (S_{11}) and gain were obtained by microwave measurement through a vector network analyzer (Agilent E8362B) connected with a standard antenna system [36, 37]. As shown in Fig. 10(a), it can be clearly seen that the actual measured resonance points obtained at 3.51 GHz, 4.7 GHz, 4.95 GHz, and 5.59 GHz are in reasonable agreement with the simulated results. Besides, the measured S_{11} below -10 dB of the proposed antenna is from 3.26 GHz to 5.84 GHz with the relative bandwidth of 56.7%, which is consistent well with the simulated one. The discrepancies between the measurement and simulation are mainly due to fabrication tolerances, installation errors, and some disturbances in the experimental environment. Fig. 10(b) presents a comparison of the measured results of the gain with the simulated ones. The measured gain is over 8 dBi on average across the whole interested frequency range. In addition, the measured peak gain is about 10.7 dBi. The trend of the measured gain vs frequency is in close compliance with the simulated result, which proves the feasibility of the design method.

The measured radiation patterns were obtained by placing the antenna at the center of the revolving stage and using a wideband horn antenna connected with an embedded intelligent platform (IPC-

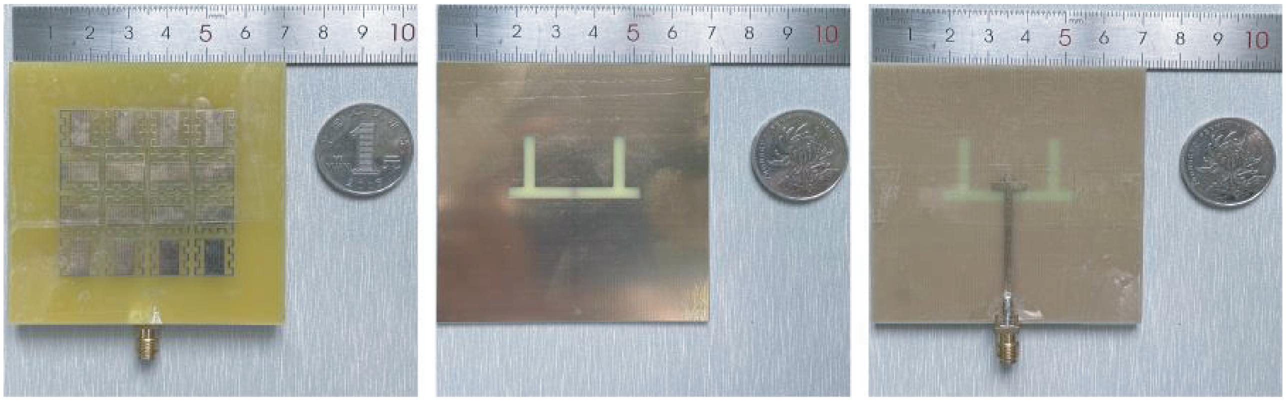

(a) (b) (c)

Figure 9. The photographs of the fabricated prototype: the front view of (a) the AMS, (b) coupled inverted π-slot structure, and (c) microstrip feed line.

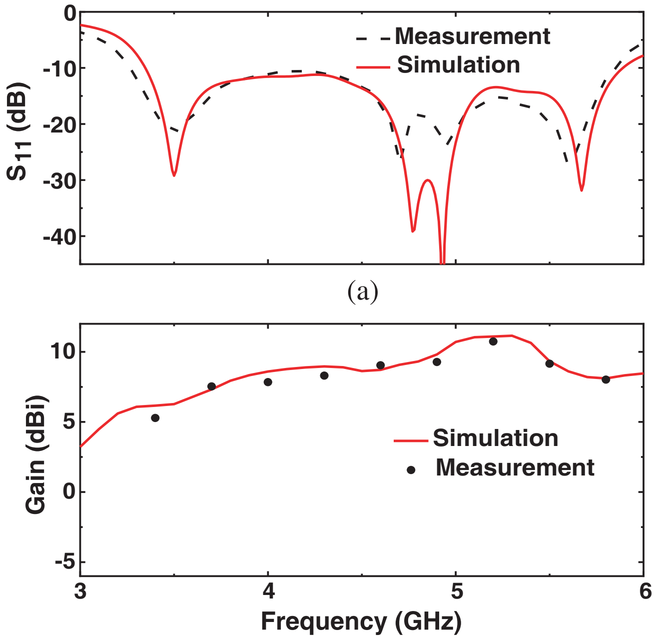

(a)

(b)

Figure 10. Comparisons of the measurement and simulation: (a) reflection coefficient (S_{11}), and (b) realized gain.

810E). The simulated and measured radiation patterns of the antenna in E-plane and H-plane at the corresponding four resonance frequency points are shown in Fig. 11. As can be seen, the radiation characteristics show good unidirectionality and stability in the operating frequencies. Although there are certain preparation and measurement tolerances, good agreement between the simulated and measured results can be observed. In addition, low cross-polarization levels of less than -16 dB can be observed in both the E-plane and H-plane. These results show the wideband, high-gain, and stable radiation characteristics of the proposed design.

To characterize the radiation properties of the proposed antenna more visually, the simulated 3D far-field patterns at four corresponding resonance points are provided in Fig. 12. The gain variation, radiation directionality, and half-power beamwidth of the proposed antenna maintain good stability under a variety of resonance and radiation modes, proving feasibility of the design method.

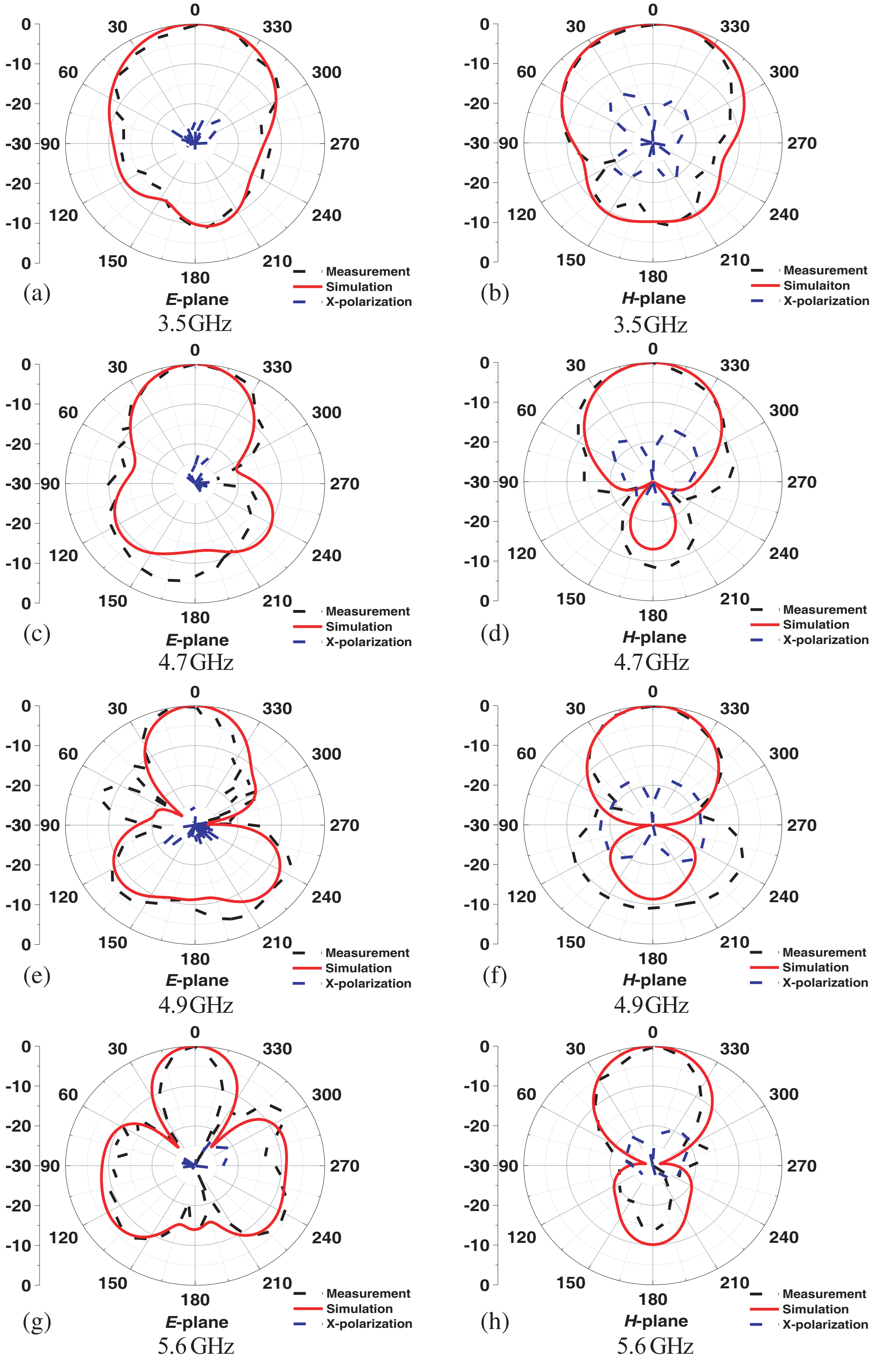

Figure 11. Measured and simulated radiation patterns of the proposed design in both (a), (c), (e), (g) *E*-plane and (b), (d), (f), (h) *H*-plane at different resonant frequencies: (a)–(b) 3.5 GHz, (c)–(d) 4.7 GHz, (e)–(f) 4.9 GHz and (g)–(h) 5.6 GHz.

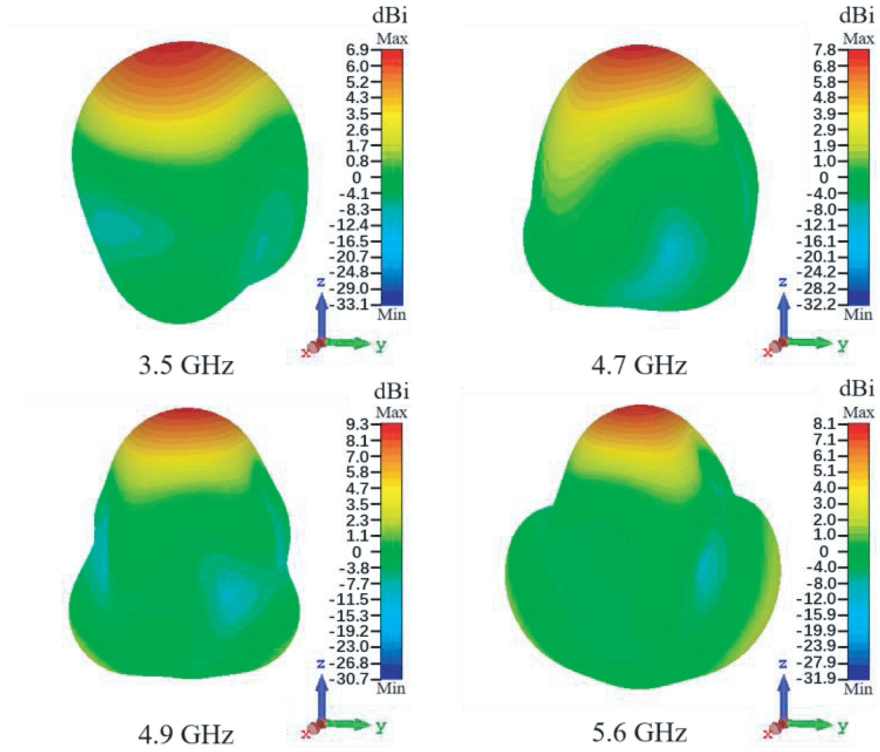

Figure 12. Simulated 3D far-field patterns of the proposed antenna at different resonant frequencies.

In order to better show the advantages of the proposed AMS-based microstrip-fed slot antenna, comparisons with various previous antenna designs are presented in Table 1, where λ is the wavelength corresponding to the center frequency of the antenna. Clearly, compared with other previous works [10, 30–32, 35], the proposed design has a lower profile while achieving a wider operating bandwidth, where the four resonant modes offer more possibilities for band expansion. This study is able to further expand on the independently tunable resonance points starting from the polarization modes. In addition, the side and rear lobe levels can also be a starting point for further optimization of the structure.

Table 1. Comparison of the proposed antenna with previous ones.

Ref.	Size	Impedance bandwidth (%)	Peak gain (dBi)	Number of resonances
[10]	$1.21\lambda_0 \times 1.21\lambda_0 \times 0.10\lambda_0$	34.7	12.3	2
[30]	$1.10\lambda_0 \times 1.10\lambda_0 \times 0.06\lambda_0$	25	9.9	2
[31]	$1.10\lambda_0 \times 1.10\lambda_0 \times 0.06\lambda_0$	28	9.8	2
[32]	$1.26\lambda_0 \times 1.26\lambda_0 \times 0.03\lambda_0$	14	10.5	2
[35]	$1.10\lambda_0 \times 1.10\lambda_0 \times 0.06\lambda_0$	44.4	10.9	3
Proposed	$1.07\lambda_0 \times 1.07\lambda_0 \times 0.06\lambda_0$	56.1	11.1	4

4. CONCLUSION

In conclusion, a wideband and high-gain microstrip-fed slot antenna based on an AMS and microstrip aperture coupled structure was proposed and demonstrated experimentally. A dual frequency resonance response to different polarization waves was achieved by etching multistage slots on a conventional square patch. A dual-mode resonance AM was constructed by rationalizing unit-cell structures along two orthogonal orientations. An additional low frequency resonance mode was introduced by etching a pair of stubs symmetrically into a horizontal slot in the center of the ground plane. When the dual-mode resonance AMS was applied to a dual-mode aperture coupled structure, the combination of the two dual-mode resonances enable wideband radiation with four adjacent resonance frequencies. Simulated and measured results show that the proposed design achieves a relative bandwidth of more than 56% and a stable gain in the operating frequency range. Compared to the previous several representative designs [10, 30–32, 35], the proposed design method enables an extended impedance bandwidth and flexible and controllable resonances. It has good scalability, and by improving on the multi-polarization method, more independently controllable resonance modes are expected to be realized, leading to further optimization of the impedance bandwidth. The proposed design meets the requirements of high data rate communication systems, covers n77, n78, and n79 frequency bands in the FR1 frequency range as well as the downlink bands with a low relative profile and small size.

ACKNOWLEDGMENT

This work is supported by the National Natural Science Foundation of China (Grant No. 51972242), the Science Fund for Creative Research Groups of the National Natural Science Foundation of Hubei Province (Grant No. 2020CFA038) and the Key Research and Development Project of Hubei Province (Grant No. 2020BAA028).

REFERENCES

1. Park, J., M. Jeong, N. Hussain, S. Rhee, S. Park, and N. Kim, "A low-profile high-gain filtering antenna for fifth generation systems based on nonuniform metasurface," *Microw. Opt. Technol. Lett.*, Vol. 61, 2513, 2019.
2. Salhi, R., M. Labidi, M. A. Boujemaa, and F. Choubani, "Dual-band microstrip patch antenna based on metamaterial refractive surface," *Appl. Phys. A — Mater.*, Vol. 123, 420, 2017.
3. Schaubert, D. H., D. M. Pozar, and A. Adrian, "Effect of microstrip antenna substrate thickness and permittivity: Comparison of theories and experiment," *IEEE T. Antenn. Propag.*, Vol. 37, 677, 1989.
4. Tian, C., Y. C. Jiao, G. Zhao, and H. Wang, "A wideband transmit array using triple-layer elements combined with cross slots and double square rings," *IEEE Antenn. Wirel. Pr.*, Vol. 16, 1561, 2017.
5. Carolina, M. S., A. P. Feresidis, and G. Goussetis, "Bandwidth enhancement of 2-D leaky-wave antennas with double-layer periodic surfaces," *IEEE T. Antenn. Propag.*, Vol. 62, 586, 2014.
6. Xu, K. D., D. T. Li, Y. H. Liu, and Q. H. Liu, "Printed quasi-yagi antennas using double dipoles and stub-loaded technique for multi-band and broadband applications," *IEEE Access*, Vol. 6, 31695, 2018.
7. Rengasamy, R., D. Dhanasekaran, C. Chakraborty, and S. Ponnan, "Modified Minkowski fractal multiband antenna with circular-shaped split-ring resonator for wireless applications," *Measurement*, Vol. 182, 109766, 2021.
8. Gupta, R. K. and J. Mukherjee, "Efficient high gain with low sidelobe level antenna structures using circular array of square parasitic patches on a superstrate layer," *Microw. Opt. Technol. Lett.*, Vol. 52, 2812, 2010.
9. Zhang, X. and L. Zhu, "Gain-enhanced patch antennas with loading of shorting pins," *IEEE T. Antenn. Propag.*, Vol. 64, 3310, 2016.
10. Bai, H., G. M. Wang, and X. J. Zou, "A wideband and multi-mode metasurface antenna with gain enhancement," *AEU — Int. J. Electron. C.*, Vol. 126, 153402, 2020.

11. Das, S. and S. Sahu, "Polarization reconfigurability enabled metamaterial inspired dielectric resonator based Fabry-Perot resonator cavity antenna with high gain and bandwidth," *Int. J. RF Microw. C. E.*, Vol. 31, e22603, 2021.
12. Cao, Y. F., Y. Cai, W. Q. Cao, B. K. Xi, Z. P. Qian, T. Wu, and L. Zhu, "Broadband and high-gain microstrip patch antenna loaded with parasitic mushroom-type structure," *IEEE Antenn. Wirel. Pr.*, Vol. 18, 1405, 2019.
13. Cheng, Y. Z., F. Chen, and H. Luo, "Plasmonic chiral metasurface absorber based on bilayer fourfold twisted semicircle nanostructure at optical frequency," *Nanoscale Res. Lett.*, Vol. 16, 12, 2021.
14. Gao, G. P., C. Yang, B. Hu, S. F. Wang, and R. F. Zhang, "Design of a high-gain and low-profile quasi-Cassegrain antenna based on metasurfaces," *IEEE Antenn. Wirel. Pr.*, Vol. 17, 1435, 2018.
15. Li, H. P., G. M. Wang, H. X. Xu, T. Cai, and J. G. Liang, "X-band phasegradient metasurface for high-gain lens antenna application," *IEEE T. Antenn. Propag.*, Vol. 63, 5144, 2015.
16. Tong, X. Y., X. B. Zhao, F. Wei, L. Xu, and R. Li, "Broadband folded reflectarray based on single-layer subwavelength elements using discrete phase control," *Int. J. Rf Microw. C. E.*, Vol. 31, e22710, 2021.
17. Yang, Z. Z., F. Liang, Y. Yi, D. S. Zhao, and B. Z. Wang, "Metasurface-based wideband, low-profile, and high-gain antenna," *IET Microw. Antenna P.*, Vol. 13, 436, 2018.
18. Zhou, E. Y., Y. Z. Cheng, F. Chen, and H. Luo, "Wideband and high-gain patch antenna with reflective focusing metasurface," *AEU — Int. J. Electron. C.*, Vol. 134, 153709, 2021.
19. Yue, T., Z. H. Jiang, and D. H. Werner, "Compact, wideband antennas enabled by interdigitated capacitor-loaded metasurfaces," *IEEE T. Antenn. Propag.*, Vol. 64, 1595, 2016.
20. Asadpor, L., G. Sharifi, and M. Rezvani, "Design of a high-gain wideband antenna using double-layer metasurface," *Microw. Opt. Technol. Lett.*, Vol. 61, 1004, 2018.
21. Majumder, L., K. Krishnamoorthy, J. Mukherjee, and K. P. Ray, "Compact broadband directive slot antenna loaded with cavities and single and double layers of metasurfaces," *IEEE T. Antenn. Propag.*, Vol. 64, 4595, 2016.
22. Ma, S. B., H. Q. Zhai, Z. C. Wei, X. Y. Zhou, L. C. Zheng, and J. X. Li, "A high-selectivity dual-polarization filtering antenna with metamaterial for 5G application," *Microw. Opt. Technol. Lett.*, Vol. 61, 63, 2018.
23. Pan, Y. M., P. F. Hu, X. Y. Zhang, and S. Y. Zheng, "A low-profile high-gain and wideband filtering antenna with metasurface," *IEEE T. Antenn. Propag.*, Vol. 64, 2010, 2016.
24. Wu, T., J. Chen, and M. J. Wang, "Multi-state circularly polarized antenna based on the polarization conversion metasurface with gain enhancement," *IEEE Access*, Vol. 8, 84660, 2020.
25. Rajanna, P. K. T., K. Rudramuni, and K. Kandasamy, "A high gain circularly polarized antenna using zero-index metamaterial," *IEEE Antenn. Wirel. Pr.*, Vol. 18, 1129, 2019.
26. Hong, T., S. Wang, Z. Y. Liu, and S. X. Gong, "RCS reduction and gain enhancement for the circularly polarized array by polarization conversion metasurface coating," *IEEE Antenn. Wirel. Pr.*, Vol. 18, 167, 2019.
27. Fan, J. P., Y. Z. Cheng, and B. He, "High-efficiency ultrathin terahertz geometric metasurface for full-space wavefront manipulation at two frequencies," *J. Phys. D: Appl. Phys.*, Vol. 54, 115101, 2021.
28. Cheng, Y. Z., J. P. Fan, H. Luo, and F. Chen, "Dual-band and high-efficiency circular polarization convertor based on anisotropic metamaterial," *IEEE Access*, Vol. 8, 7615, 2019.
29. Dwivedi, A. K., A. Sharma, A. K. Singh, and V. Singh, "Metamaterial inspired dielectric resonator MIMO antenna for isolation enhancement and linear to circular polarization of waves," *Measurement*, Vol. 182, 109681, 2021.
30. Liu, W., Z. N. Chen, and X. M. Qing, "Metamaterial-based low-profile broadband mushroom antenna," *IEEE T. Antenn. Propag.*, Vol. 62, 1165, 2013.
31. Liu, W., Z. N. Chen, and X. M. Qing, "Metamaterial-based low-profile broadband aperture-coupled grid-slotted patch antenna," *IEEE T. Antenn. Propag.*, Vol. 63, 3325, 2015.

32. Majumder, B., K. Kandasamy, J. Mukherjee, and K. P. Ray, “Wideband compact directive metasurface enabled pair of slot antennas,” *Electron. Lett.*, Vol. 51, 1310, 2015.
33. Bai, H. and G. M. Wang, “A multistate high gain antenna based on metasurface,” *Int. J. RF Microw. C. E.*, Vol. 30, e22330, 2020.
34. Sievenpiper, D., L. J. Zhang, and R. F. J. Broas, “High-impedance electromagnetic surfaces with a forbidden frequency band,” *IEEE T. Microw. Theory*, Vol. 47, 2059, 1999.
35. Chen, D. X., W. C. Yang, Q. Xue, and W. Q. Che, “Wideband high-gain multiresonance antenna based on polarization-dependent metasurface,” *Microw. Opt. Technol. Lett.*, Vol. 63, 638, 2021.
36. Wang, J., Y. Cheng, H. Luo, F. Chen, and L. Wu, “High-gain bidirectional radiative circularly polarized antenna based on focusing metasurface,” *Int. J. Electron. Commun. (AEÜ)*, Vol. 151, 154222, 2022.
37. Cheng, Y. Z., J. Yu, and X. Li, “Tri-band high-efficiency circular polarization convertor based on double-split-ring resonator structures,” *Appl. Phys. B — Lasers O.*, Vol. 128, 1, 2022.